J. Fluid Mech. (2013), *vol.* 716, *pp.* 638–657. © Cambridge University Press 2013
doi:10.1017/jfm.2012.564

An experimental study of edge effects on rotating-disk transition

Shintaro Imayama[1,†], **P. Henrik Alfredsson**[1] **and R. J. Lingwood**[1,2]

[1]Linné Flow Centre, KTH Mechanics, SE-100 44 Stockholm, Sweden
[2]Institute of Continuing Education, University of Cambridge, Madingley Hall, Madingley, Cambridge CB23 8AQ, UK

(Received 19 June 2012; revised 8 November 2012; accepted 13 November 2012)

The onset of transition for the rotating-disk flow was identified by Lingwood (*J. Fluid. Mech.*, vol. 299, 1995, pp. 17–33) as being highly reproducible, which motivated her to look for absolute instability of the boundary-layer flow; the flow was found to be locally absolutely unstable above a Reynolds number of 507. Global instability, if associated with laminar–turbulent transition, implies that the onset of transition should be highly repeatable across different experimental facilities. While it has previously been shown that local absolute instability does not necessarily lead to linear global instability: Healey (*J. Fluid. Mech.*, vol. 663, 2010, pp. 148–159) has shown, using the linearized complex Ginzburg–Landau equation, that if the finite nature of the flow domain is accounted for, then local absolute instability can give rise to linear global instability and lead directly to a nonlinear global mode. Healey (*J. Fluid. Mech.*, vol. 663, 2010, pp. 148–159) also showed that there is a weak stabilizing effect as the steep front to the nonlinear global mode approaches the edge of the disk, and suggested that this might explain some reports of slightly higher transition Reynolds numbers, when located close to the edge. Here we look closely at the effects the edge of the disk have on laminar–turbulent transition of the rotating-disk boundary-layer flow. We present data for three different edge configurations and various edge Reynolds numbers, which show no obvious variation in the transition Reynolds number due to proximity to the edge of the disk. These data, together with the application (as far as possible) of a consistent definition for the onset of transition to others' results, reduce the already relatively small scatter in reported transition Reynolds numbers, suggesting even greater reproducibility than previously thought for 'clean' disk experiments. The present results suggest that the finite nature of the disk, present in all real experiments, may indeed, as Healey (*J. Fluid. Mech.*, vol. 663, 2010, pp. 148–159) suggests, lead to linear global instability as a first step in the onset of transition but we have not been able to verify a correlation between the transition Reynolds number and edge Reynolds number.

Key words: absolute/convective instability, boundary layer stability, transition to turbulence

† Email address for correspondence: shintaro@mech.kth.se

https://doi.org/10.1017/jfm.2012.564 Published online by Cambridge University Press

1. Introduction

This paper is concerned with an incompressible rotating-disk boundary-layer flow without any imposed flow. The laminar boundary layer established on a rotating disk has a three-dimensional profile with an inflection point in the radial direction. For an infinite disk rotating in an otherwise quiescent fluid there is an exact similarity solution, first described by von Kármán (1921). The Rossby number for the von Kármán flow is $Ro = -1$, as defined, for example, by Lingwood & Garrett (2011). The instability and transition of the rotating-disk flow has been investigated starting with Theodorsen & Regier (1944) and Smith (1947) who noticed fluctuations in the boundary layer on the rotating disk using a hot-wire probe. Visualization studies performed by Gregory, Stuart & Walker (1955) and Kohama (1984) showed 28–32 stationary (in the rotating frame) vortices in the unstable region. Experiments by Kobayashi, Kohama & Takamadate (1980) and Malik, Wilkinson & Orszag (1981) using hot-wire anemometry both gave the Reynolds number, R, for the onset of convective instability for stationary modes slightly below 300, where $R = r^*(\Omega^*/\nu^*)^{1/2}$, r^* is the radius of the disk at the measurement position, Ω^* is the rotational speed of the disk, ν^* is the kinematic viscosity of the fluid and * denotes a dimensional quantity. Local linear stability analyses (Lingwood 1995) also reveal this unstable region with two different modes: an inviscid instability mode, called Type I, caused by an inflection point in the radial velocity component, and a viscous instability mode, called Type II, caused by streamwise curvature and Coriolis effects. Type II stationary disturbances have smaller linear growth rates than Type I.

There are other stable modes, and one of these, henceforth called Type III, was shown by Lingwood (1995, 1997) to coalesce with Type I above $R_{CA} = 507$ for a range of non-zero frequencies, i.e. for certain disturbances travelling with respect to the disk rotation. Here R_{CA} is the critical Reynolds number for onset of local absolute instability. The absolute instability is an inviscid mechanism and Lingwood (1995) suggested it has a role in triggering nonlinearity, related to the onset of transition to turbulence. By introducing impulsive excitation to the rotating-disk boundary-layer flow, she confirmed experimentally the absolute instability (above about $R = 507$) by tracking the trajectory of the excited wavepacket (Lingwood 1996) and showed the development of nonlinearity and the onset of the transition process from there, resulting in a fully turbulent flow at about $R = 600$–650. Theodorsen & Regier (1944), Kobayashi *et al.* (1980) and Othman & Corke (2006) performed careful experiments, and gave transition Reynolds numbers in the range 539–566, numbers that are higher than the critical absolute Reynolds number. Davies & Carpenter (2003) performed direct numerical simulations (DNSs) solving the linearized Navier–Stokes equations and suggested that the convective behaviour eventually prevails even for strongly locally absolutely unstable regions and concluded that the absolute instability does not produce a linear amplified global mode.

As shown by Huerre & Monkewitz (1990), the presence of a local absolute instability does not necessarily give rise to a linear global instability. Taking this point into account, Pier (2003) suggested that a nonlinear approach is required to explain the self-sustained behaviour of the rotating-disk flow. He suggested that the rotating-disk boundary layer has a primary nonlinear global mode fixed by the local absolute instability, which has a secondary absolute instability that triggers the transition to turbulence. In fact, Kohama (1984) presented smoke-flow visualizations that show a secondary instability on the stationary primary vortices, which takes the form of 'ring-like vortices that occur on the surfaces of each spiral vortices (*sic*)'. Furthermore, Imayama, Alfredsson & Lingwood (2012) represented the vertical structure of the

https://doi.org/10.1017/jfm.2012.564 Published online by Cambridge University Press

Study	R_t	Method
Theodorsen & Regier (1944)	557	Hot wire
Gregory *et al.* (1955)	533 : (520–547)	Visual, China clay
Cobb & Saunders (1956)	490	Heat transfer
Gregory & Walker (1960)	524	Pressure probe
Chin & Litt (1972)	570 : (548–592)	Mass transfer
Fedorov *et al.* (1976)	515	Visual, naphthalene
Clarkson, Chin & Shacter (1980)	621 : (562–680)	Visual, dye
Kobayashi *et al.* (1980)	566	Hot wire
Malik *et al.* (1981)	520 : (513–526)	Hot wire
Wilkinson & Malik (1985)	550 : (543–556)	Hot wire
Lingwood (1996)	508 : (502–514)	Hot wire
Othman & Corke (2006)	539	Hot wire

TABLE 1. Experimental transition Reynolds numbers, R_t, given in previous studies using various experimental techniques (as defined in the original studies).

vortices that show signs of secondary instability at $R = 550$–570 just before the turbulent breakdown region. However, the behaviour of the secondary instability and also its relation to the primary absolute instability are not fully understood as yet.

Othman & Corke (2006) performed experiments similar to those of Lingwood (1996) but used both a low-amplitude and a high-amplitude initial pulse-jet excitation to create a wavepacket disturbance in the boundary-layer flow. In contrast to Lingwood (1996) the trailing edge of the wavepacket did not become fixed at R_{CA} with the low-amplitude initial disturbance, hence the results agree well with the linearized DNSs of Davies & Carpenter (2003). However, the amplitude of the wavepacket with the high-amplitude initial disturbance compares better with the result of Lingwood (1996), although it is not certain that the trailing edge of the wavepacket becomes fixed at R_{CA}. However, Imayama *et al.* (2012) suggested that the change in slope at around $R = 545$ in disturbance growth (their figure 5) could correspond to the so-called 'secondary front' suggested by Viaud, Serre & Chomaz (2011), leading to a cascade of absolutely unstable secondary instabilities and transition to turbulence. This evidence given by Imayama *et al.* (2012) is perhaps the first experimental validation of secondary absolute instability of the primary nonlinear (steep-fronted) global mode shown in the DNS results of Viaud *et al.* (2011).

Albeit relatively small compared with other boundary-layer flows, Healey (2010) recognized the scatter of experimentally observed transition Reynolds number, R_t, reported by previous authors, as can be seen in table 1, and suggested that the proximity of the edge of the disk to the transition region is important; an effect not captured by standard analyses assuming an infinite disk radius. Davies & Carpenter (2003) carried out DNSs of the linearized equations and showed that local absolute instability does not produce a linear global instability but, as Healey (2010) explains, they disregarded upstream propagation of waves from the edge boundary as a spurious numerical artefact and so stopped their simulations before upstream propagating waves reached the domain of interest. Healey (2010) argued that, based on investigations of the linearized complex Ginzburg–Landau equation, the transition Reynolds number should depend on the Reynolds number at the edge of the disk, R_{edge}, where $R_{edge} = r_d^*(\Omega^*/\nu^{*1/2}$, r_d^* is the actual radius of the disk. Contradicting Davies & Carpenter (2003), Healey's (2010) theory predicts, regardless of the background

https://doi.org/10.1017/jfm.2012.564 Published online by Cambridge University Press

disturbance level, that at leading order (i.e. when the flow is weakly inhomogeneous in the radial direction) there can be a linear global instability when there is local absolute instability at the edge of the disk. Healey (2010) also added a simple nonlinear term to the complex Ginzburg–Landau equation to look at the effect on the appearance of a steep-fronted nonlinear global mode, showing that there is a weak stabilizing correction in the nonlinear analysis to the Reynolds number for global instability when the steep-fronted global mode is close to the disk edge. Figure 7(*b*) of Healey (2010) shows the variation in the experimentally observed transition Reynolds number depending on the edge Reynolds number compared with his theoretical prediction.

As suggested by Healey (2010), experiments have been undertaken to investigate the effect of the edge of the disk on the instability and transition process, and these results are presented here. The study includes measurements of the flow with a range of edge Reynolds numbers and several different edge conditions. No obvious effect of the proximity of the disk edge or of the nature of the edge condition on the transition Reynolds number were observed. In addition, it is suggested that the scatter of the transition Reynolds number reported by previous authors is largely explained by their different definitions of what constitutes transition.

2. Experimental set-up and procedure

The experimental set-up is identical to that used by Imayama *et al.* (2012) which is a modified version of Lingwood's (1996) apparatus. A new disk made of glass with a thickness of 24 mm and a diameter of 474 mm has been mounted on the original aluminium-alloy disk, which is connected to a DC-servo motor via a vertical shaft. A pressurized air bearing ensures that the vibrations of the disk are small. At the edge of the disk the glass disk is ground down approximately 1.5 mm with a 45° angle, and the radius of the working side of the glass plate is hence $r_d^* = 235.5$ mm . The surface of the glass disk is polished resulting in a surface roughness of less than 1 μm; the rotational imbalance is less than 10 μm at the edge and smaller at the centre region of the glass disk.

To investigate the effect on the transition process caused by the disk edge condition, different conditions have been considered. Figure 1 shows the three different edge conditions. Figure 1(*a*) shows the 'open-type', which has no extended plate or cover, figure 1(*b*) shows the 'ring-type', where there is a steel ring mounted below the surface of the disk covering eight aluminum clamps fixing the glass disk to the aluminum-alloy disk. These clamps, which are below the vertical edge of the glass disk, generate a disturbances field with eight oscillations per rotation of the disk if not covered. The ring is mounted around them to eliminate their contribution to the flow disturbance field. The ring itself does not rotate and the horizontal gap between the ring and glass disk is less than 1 mm. The edge of the glass disk is still exposed in a similar way to the open-type edge condition because the top of the ring is located 11 mm vertically below the disk surface. The third case, figure 1(*c*) is called 'plate type', which consists of a non-rotational extended annular plate made of wood with an outside diameter of 900 mm mounted around the glass disk. This extended plate reduces the effects of the eight aluminum fixing components and also the effects of noise coming from the air bearing and DC-servo motor. Vertically the disk surface and plate are approximately flush and the horizontal gap between the disk and plate is less than 1 mm.

The velocity measurements have been performed using a hot-wire probe with a single sensor. The sensor is made of platinum, with a diameter of 5 μm and 1 mm in

https://doi.org/10.1017/jfm.2012.564 Published online by Cambridge University Press

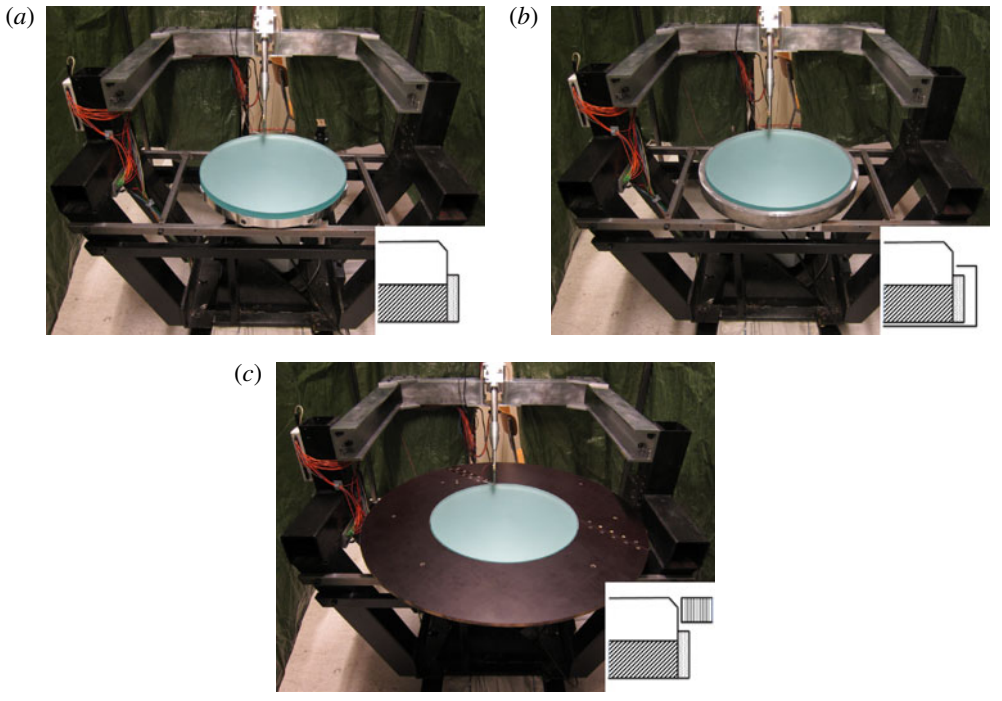


FIGURE 1. (Colour online) Three edge configurations. The pictures at lower right of each photograph show a cross-sectional sketch of each disk edge configuration (not to scale). The white, dark grey and light grey part in each sketch presents the glass disk, aluminium-alloy disk and one of the eight aluminium clamps, respectively. The solid line in (*a*) shows open type, in (*b*) indicates a steel ring and the upright component and in (*c*) shows the wooden annular plate.

length, being operated by a constant-temperature anemometer (CTA) with an overheat ratio of 0.8. The sensor is mainly sensitive to the azimuthal velocity component since its sensing element is oriented in the radial direction. The positioning of the hot-wire probe is remotely controlled by a two-axis traversing mechanism which is oriented at 45° to the vertical to limit disturbance of the incoming downward axial flow. The calibration of the hot wire is performed on the rotating disk using the azimuthal laminar velocity profile and the calibration data are fitted using a modified King's law (Johansson & Alfredsson 1982).

The experimental conditions are shown in table 2. The Reynolds number was varied using two methods: (i) varying the rotational disk speed and keeping the probe at a fixed radial position for the PO, PR, PP, IP00 cases; and (ii) varying the radial position of the probe at a fixed rotational disk speed for other cases. The measurements were performed taking extreme care with the glass surface. Before rotating the disk, the surface of glass disk was cleaned with acetone and carefully checked that there were no visible dust particles on the surface. The Reynolds numbers for IO, IR and IP were changed every 5 ΔR across the measurement range, where ΔR is the unit Reynolds number. All measurements are in the laboratory frame rather than the disk's rotational frame.

For the IO, IR and IP cases (excluding the IP00 case), the Reynolds number was changed by varying the radius at which the measurements were taken. The

https://doi.org/10.1017/jfm.2012.564 Published online by Cambridge University Press

Case	Edge	Mode	R	R_{edge}	r^* (mm)	Ω^* (rpm)	z
PO	Open	Speed	430–630	512–749	198	683–1465	0.4–16(26)
PR	Ring	Speed	430–630	511–749	198	675–1455	0.4–16(26)
PP	Plate	Speed	430–630	512–749	198	690–1480	0.4–16(26)
IP00	Plate	Speed	360–640	428–763	198	486–1542	1.3
IO01	Open	Radius	360–540	551	154–231	800	1.3
IO02	Open	Radius	360–565	577	147–231	865	1.3
IO03	Open	Radius	360–605	615	138–231	1000	1.3
IO04	Open	Radius	360–700	730	116–226	1400	1.3
IR01	Ring	Radius	360–540	552	154–231	800	1.3
IR02	Ring	Radius	360–565	576	147–231	860	1.3
IR03	Ring	Radius	360–605	615	138–232	982	1.3
IR04	Ring	Radius	360–700	729	116–226	1380	1.3
IP01	Plate	Radius	360–540	555	153–229	800	1.3
IP02	Plate	Radius	360–565	577	147–231	860	1.3
IP03	Plate	Radius	360–605	618	137–231	1000	1.3
IP04	Plate	Radius	360–700	731	116–226	1400	1.3

TABLE 2. Experimental conditions. 'Edge' indicates three kinds of edge conditions, see figure 1. 'Mode' indicates the Reynolds number change method (Speed: Reynolds number is changed by varying the rotational speed of the glass disk; Radius: Reynolds number is changed by varying the radius of the hot-wire position). Here, r^* is a local radius of the hot wire and $z(=z^*\,(\Omega^*/\nu^*)^{1/2})$ is the normalized wall-normal position of the hot wire, respectively.

maximum measurement Reynolds number for these cases does not reach the edge Reynolds number exactly shown in table 2, i.e. the maximum measurement Reynolds number in IO01 is 540 despite $R_{edge} = 551$. This is because the mean flow field is disturbed very close to the disk edge. Figure 2 shows the normalized azimuthal velocity $V(=V^*/(r^*\Omega^*))$ at a constant height and each constant rotational speed. Within ~5 mm of the outer edge, the normalized azimuthal velocity suddenly drops, and so data measured this close to the outer edge were removed from the following results and discussions.

3. Results

3.1. *Azimuthal mean velocity profile*

The azimuthal mean velocity profiles with three different edge conditions are shown in figure 3. The Reynolds numbers for these velocity-profile measurements were changed by varying the rotational speeds, and these results correspond to cases PO, PR and PP with R_{edge} given by table 2. Figure 3(*a–c*) show the measured mean azimuthal velocity for each of the three edge types at different Reynolds numbers. For these subplots, the measurement Reynolds number is increased by increasing the rotational speed of the disk, while maintaining a constant radial position for the hot wire, and therefore the edge Reynolds number also increases with the measurement Reynolds numbers; see table 2. Figure 3(*d*) compares the mean azimuthal velocity profiles for three Reynolds numbers (470, 510 and 550) for constant edge Reynolds number (559, 606 and 654, respectively) across the three edge types. Figure 3(*e–g*) show v_{rms} profiles for the same three data sets shown in figure 3(*d*), where v_{rms} is defined as the non-dimensional intensity of the azimuthal velocity fluctuation ($v_{rms} = v^*_{rms}/(r^*\Omega^*)$). Figure 3 shows that the laminar mean azimuthal velocity profiles for the three edge types are,

https://doi.org/10.1017/jfm.2012.564 Published online by Cambridge University Press

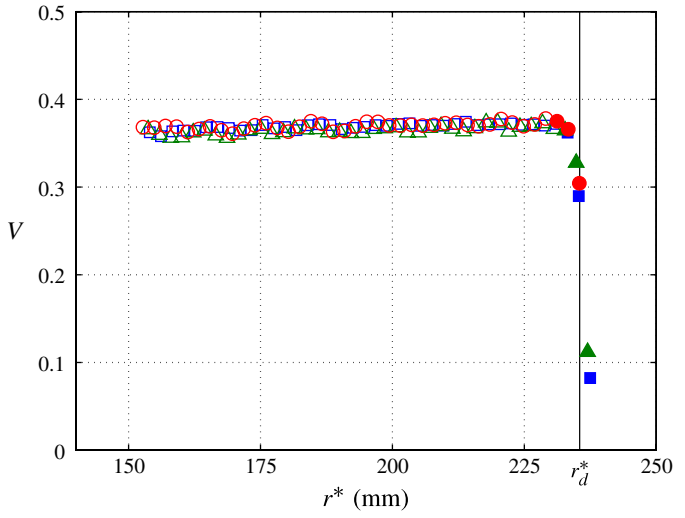


FIGURE 2. (Colour online) Mean velocity normalized by the wall velocity of: □, IO01; △, IR01; and ○, IP01; measured at $z = 1.3$ as function of r^*. The filled data points indicate removed data from the analysis, because V is reduced suddenly due to the proximity of the edge of the disk. The solid line shows the radius of the actual glass disk r_d^*.

within the limitations of experimental accuracy, unaffected by the edge conditions, i.e. consideration of the onset of nonlinearity and laminar–turbulent transition is undertaken in the present study for the same laminar base flow irrespective of the edge conditions. For Reynolds numbers in the range $R = 430$–510 and for all edge conditions, the azimuthal mean profiles measured by the hot wire correspond well to the theoretical laminar profile given as a solid line. The measured data far away from the disk have slight deviations from the solid line due to the smallness of the azimuthal velocity where the modified King's law does not fit the calibration data well. Between $R = 510$ and 550 the mean azimuthal velocity is affected by the nonlinear influence of the disturbances growth and begins to deviate from the theoretical laminar profile for all three different edge conditions, see small sections of figure 3(*a–d*). The v_{rms} profiles in figure 3(*e–g*) show the appearance of well-defined maxima at approximately $z = 1.3$ and $R = 510$ that increase in amplitude with Reynolds number. At $R = 470$, figure 3(*e*) shows the background-noise level with a maximum amplitude of approximately 6×10^{-3} for the open type; the open type is expected to show the largest background-noise level due to the unmasked influence of the disk fixings (see § 3.2). At $R = 510$, figure 3(*f*), the amplitudes of the emerging maxima in v_{rms} are consistent for the three edge types (with constant edge Reynolds number of 606) at approximately 8×10^{-3}. After the onset of nonlinearity, between $R = 510$ and 630 (here the maxima in v_{rms} are ∼10 times the level at $R = 510$), the plate type has larger deviations from the laminar mean flow than the other two cases. At $R = 630$, the velocity profile is almost fully turbulent with a dramatically increased boundary-layer thickness and a larger velocity gradient close to the wall.

3.2. *Azimuthal fluctuation velocity profile*

In figure 4 the growth of disturbances v_{rms} is shown as a function of Reynolds number. The measurements were performed at a constant height $z = 1.3$ because,

https://doi.org/10.1017/jfm.2012.564 Published online by Cambridge University Press

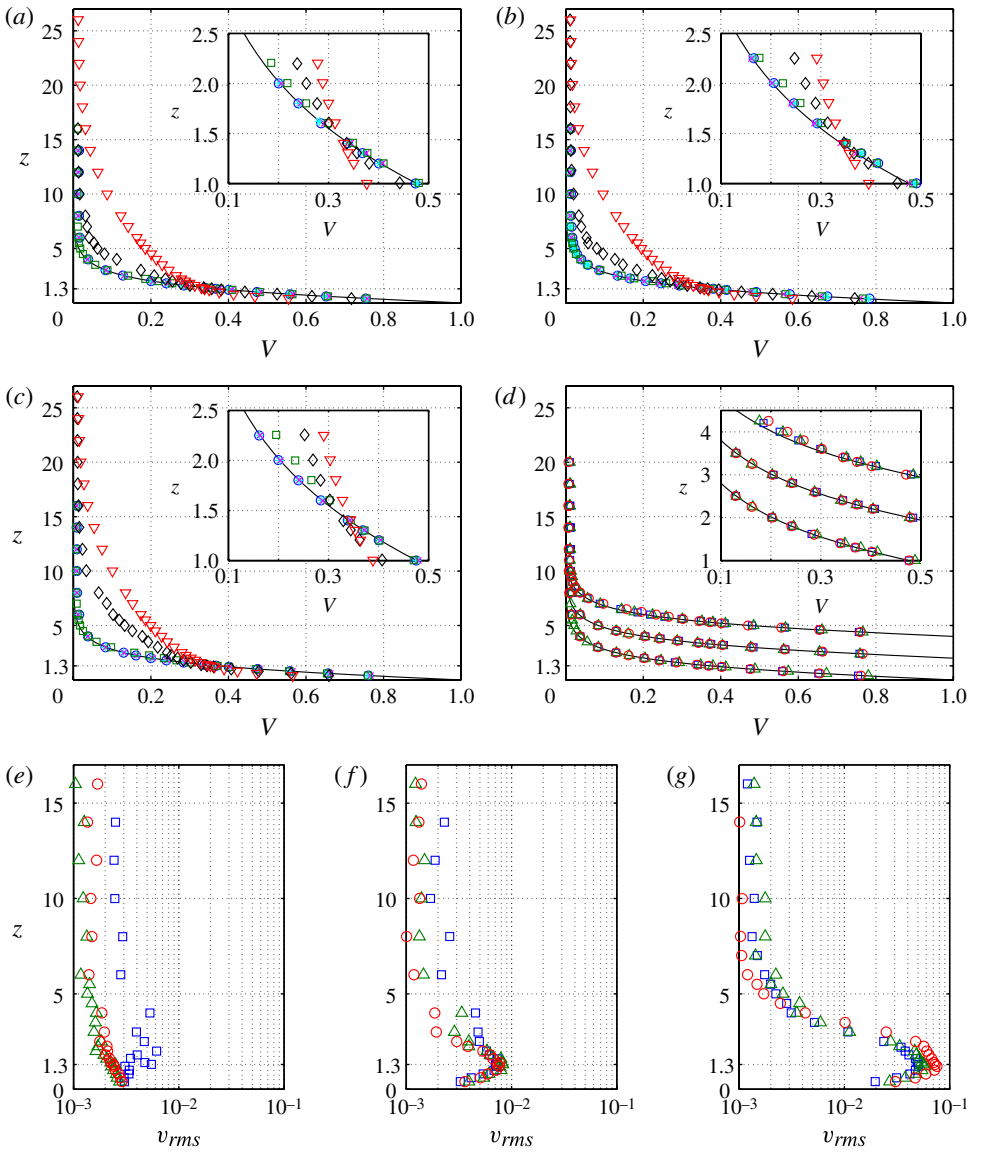


FIGURE 3. (*a–c*) Mean azimuthal velocity profiles with three different edge conditions at: ○, $R = 430$; ∗, 470; ×, 510; □, 550; ◇, 590; ▽, 630. (*d*) Mean azimuthal velocity profiles for three Reynolds numbers (470, 510 and 550) arranged in ascending order with an upwards vertical offset for presentational purposes; each of the three data sets compares the profiles for constant edge Reynolds number (559, 606 and 654, respectively) across the three edge types: □, open type; △, ring type; ○, plate type. (*e–g*) The v_{rms} profiles for the same three data sets shown in (*d*). The solid lines in (*a–d*) is the laminar theory profile, and the small figures inside the main figures show magnified regions of the velocity profiles to highlight any deviation in the mean flow: (*a*) PO case; (*b*) PR case; (*c*) PP case; (*d*) PO, PR, PP cases; (*e*) PO, PR, PP cases ($R = 470$); (*f*) PO, PR, PP cases ($R = 510$); (*g*) PO, PR, PP cases ($R = 550$).

https://doi.org/10.1017/jfm.2012.564 Published online by Cambridge University Press

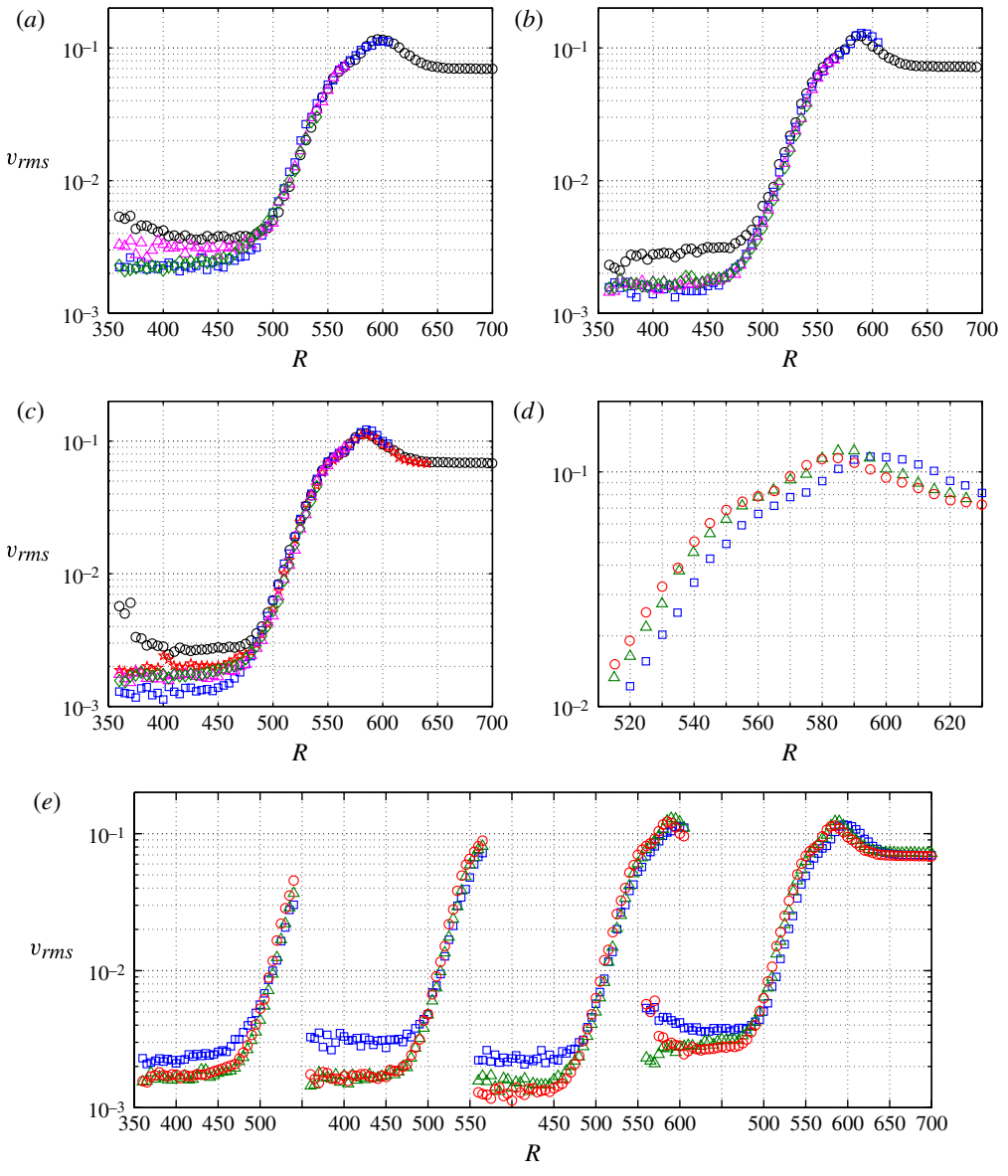


FIGURE 4. The v_{rms} values measured at $z = 1.3$ for various edge conditions and edge Reynolds number. (*a–c*) The v_{rms} values in different edge Reynolds numbers at each edge condition. The symbols indicate: ☆, 00; ◇, 01; △, 02; □, 03; ○, 04 cases, respectively, where 00–04 cases are described in table 2. (*d*) An enlargement of region of maximum v_{rms} for the final example in (*e*), i.e. for IO04, IR04, IP04. (*e*) The v_{rms} values measured at $z = 1.3$ comparing the three edge types at four approximately constant edge Reynolds numbers, from left to right: IO01, IR01, IP01, with $R_{edge} = 551, 552, 555$, respectively; IO02, IR02, IP02, with $R_{edge} = 577, 576, 577$, respectively; IO03, IR03, IP03, with $R_{edge} = 615, 615, 618$, respectively; and IO04, IR04, IP04, with $R_{edge} = 730, 729, 731$, respectively. The symbols used for the three edge types in (*d,e*) are the same as for figure 3, i.e. □, open type; △, ring type; ○, plate type: (*a*) IO case; (*b*) IR case; (*c*) IP case; (*d*) IO04, IR04, IP04 cases; (*e*) (IO01, IR01, IP01), (IO02, IR02, IP02), (IO03, IR03, IP03), (IO04, IR04, IP04) cases.

https://doi.org/10.1017/jfm.2012.564 Published online by Cambridge University Press

in the unstable region, v_{rms} has a maximum around that position; see, for example, figure 3(f) in Imayama *et al.* (2012). Figure 4(a–c) show IO01-04, IR01-04 and IP00-04 (given by table 2); for all cases apart from IP00 (in figure 4c for the plate type), the measurement Reynolds number was changed by varying the radial position of the hot wire at constant disk rotation, which means that the edge Reynolds number is constant for any particular case shown (apart from IP00). Figure 4(e) compares v_{rms} for the three edge types at four approximately constant edge Reynolds numbers, i.e. comparing IO01 with IR01 and IP01; IO02 with IR02 and IP02; IO03 with IR03 and IP03; and IO04 with IR04 and IP04. The maximum variation in the edge Reynolds number for any one of these four comparisons is less than 1 %. The highest measurement Reynolds number for each of the four sets of data in figure 4(e) corresponds to the near-edge position of 540, 565, 605 and 700, respectively. Figure 4(d) shows an enlargement of the region of maximum v_{rms} from the final example in figure 4(e), i.e. for IO04, IR04, IP04.

At low Reynolds number $R \lesssim 480$, different background-noise levels were measured depending on both the edge type (shown by each of figure 4a–c) and edge Reynolds number (shown by figure 4e). In all of these cases, the experiments with the highest rotational speed (IO04, IR04, IP04) have the largest background-noise levels. This is probably due to higher levels of vibration of the traverse and disk at higher rotational speeds. However, the lowest background-noise levels are observed for IO03, IR03 and IP03. This is perhaps because compared with the measurements performed in cases IO01-02, IR01-02 and IP01-02 those started from smaller radial positions where the imbalance of the disk is smaller, and the rotational speeds are smaller than IO04, IR04 and IP04. All of the measurements for the open-type have larger background-noise levels at $z = 1.3$ compared with the ring type and plate type. This is because the eight aluminium components that connect the glass disk to the aluminum-alloy disk disturb the flow contributing to the background noise. In the ring-type and plate-type cases these eight aluminum components are masked by the ring cover and wooden annular plate, respectively, see figure 1.

At $R \lesssim 480$ the background-noise level is relatively high compared with the amplitude of the convectively unstable disturbances. However, at $R > 480$ the flow disturbances start to exceed the background level and the exponential growth of v_{rms} is observed up to $R = 585$–595. At $R = 510$, figure 3(f) shows that the agreement between the different cases is good, which suggests that the edge conditions have little if any effect on the onset of transition, and throughout the exponential growth regions the cases match within $10\Delta R$ for all edge conditions, as shown by figure 4(d), which exhibits the largest variation between the different edge types for constant edge Reynolds number. This comparison also shows the largest variation above $R = 595$ of $\sim 15\Delta R$. A change in the exponential growth rate is observed at $R = 545$–555, which could be evidence of a 'secondary front' as described by Viaud *et al.* (2011). These results suggest three things about the transition process of the rotating disk boundary layer. First, the background disturbance sources from outside the boundary layer do not affect the transition process significantly in these cases. Second, differences in the edge configuration, namely whether there is an extended annual plate or a ring around the glass disk or not does not have a significant effect. Third, the data with different edge Reynolds numbers match closely, especially around the onset of nonlinearity and transition, which suggests the edge Reynolds number does not affect the onset of transition significantly. Further results will be considered in the following sections to corroborate these findings.

https://doi.org/10.1017/jfm.2012.564 Published online by Cambridge University Press

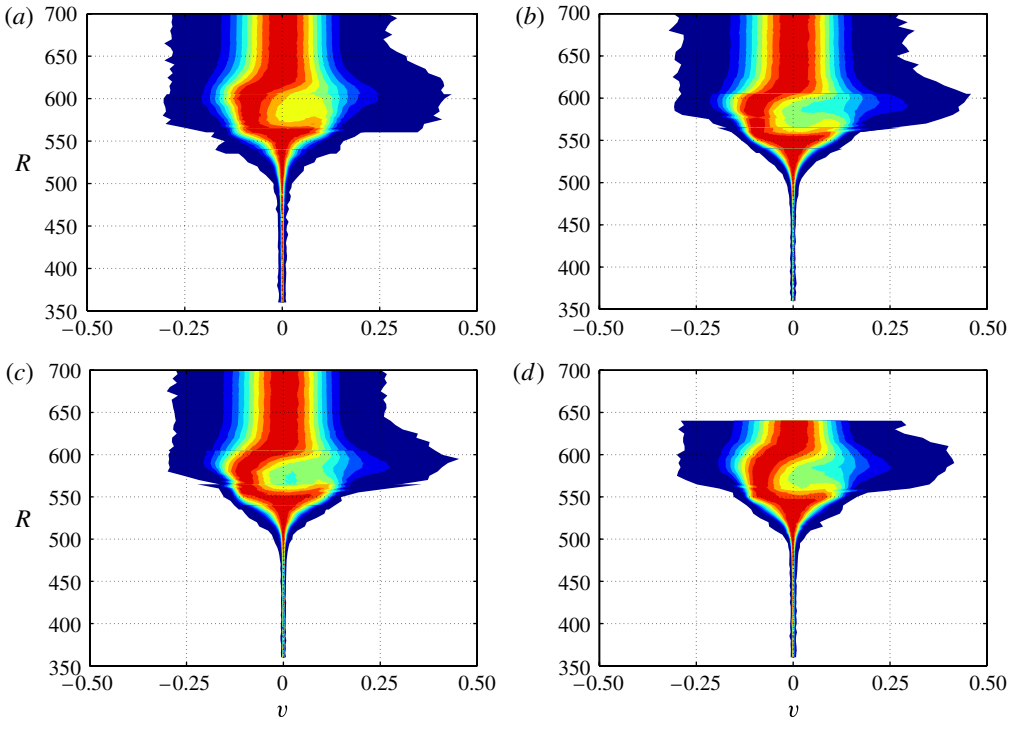


FIGURE 5. Probability distribution functions of the instantaneous azimuthal fluctuation velocity v at $z = 1.3$ normalized by the wall speed with various edge conditions and the two different modes of changing the measurement Reynolds number, i.e. by varying radial position or by varying rotational speed. Filled contours indicate 10, 20, 30, 40, 50, 60, 70, 80 and 90 % of the local p.d.f. value: (*a*) open type; (*b*) ring type; (*c*) plate type; (*d*) plate type (IP00).

3.3. *Probability density function profile*

Imayama *et al.* (2012) showed that the probability density function (p.d.f.) map of the instantaneous azimuthal velocity fluctuations could be used to gain a better insight into the different stages of the transition process, in particular how the transition process progresses with increasing Reynolds number. A similar approach was taken by Le Gal (1992) for a quantitative statistical analysis of velocity fluctuations related to a transition process. The p.d.f. of a fluctuating velocity time series gives a measure of the relative likelihood for the amplitude of the fluctuations to take on a given value. For example, a random signal would give a symmetric, near-Gaussian p.d.f. As was shown by Imayama *et al.* (2012) the exponential growth is seen as a symmetric widening of the p.d.f., after which at a certain Reynolds number the p.d.f. changes character and becomes strongly asymmetric. Here, following this idea, p.d.f. maps are given for the instantaneous azimuthal velocity time series as function of the Reynolds numbers for different edge conditions. Thus, the maps are formed by piecing together p.d.f.s of time series measured at sequential Reynolds numbers (all computed for 60 s of data, i.e. between 486 and 1542 rotations of the disk, at each measuring location).

Figure 5 shows the resulting colour contour plot of the p.d.f. for the same data as in figure 4. The open, ring and plate types in figure 5(*a–c*) represent the superposition of different edge conditions, namely IO01, IR01 and IP01 are used for $360 \leqslant R \leqslant 540$,

https://doi.org/10.1017/jfm.2012.564 Published online by Cambridge University Press

IO02, IR02 and IP02 are used for $540 < R \leqslant 565$, IO03, IR03 and IP03 are used for $565 < R \leqslant 605$ and IO04, IR04 and IP04 are used for $605 < R \leqslant 700$. Figure 5(*d*) shows the single plate-type (IP00) case. If the transition process were affected by the edge Reynolds number, then the superposition p.d.f. map would include significant discontinuities. However, figure 4 indicates continuous and similar p.d.f. trends as a function of the measurement Reynolds number. The ring-type case in figure 5(*b*) has a slightly discontinuous region at $R = 605$, however the gap is less than $10\Delta R$.

In figure 5 the p.d.f.s are narrow and constant at $R < 475$. The open-type case is slightly broader at low Reynolds number compared with the other edge conditions due to higher background-noise levels. At $R \geqslant 475$ the p.d.f. spreads exponentially up to about $R = 550$, which then corresponds to the secondary front as shown figure 4. At $R = 550$, the structure of the p.d.f. changes dramatically and becomes strongly skewed. This is indicative of secondary instability, as also shown by figure 7 in Imayama *et al.* (2012), which presents p.d.f. maps of instantaneous velocity fluctuations at fixed Reynolds numbers but measured at varying distance from the disk, showing the changing z-structure of the disturbance field in the transitional regime much more clearly than the spectral and root mean square (r.m.s.) distributions (also presented there). At around $R = 600$ in figure 5, the skewed p.d.f. starts to disappear and the positive deviation of v has its maximum. The almost symmetric p.d.f. above $R = 650$–660 indicates that the flow has reached a fully developed turbulent state.

4. Discussion of results

The present results as shown in figures 4 and 5 show that the development of the flow seems to be independent of both the edge Reynolds number and edge conditions. Here, the focus is on the transition Reynolds number and the need to consider the (albeit relatively small) scatter of the transition Reynolds number reported by the previous authors and the results of Healey (2010), which propose: first, that if the finite nature of the flow domain is accounted for, i.e. the finite radius of the disk, then local absolute instability can give rise to linear global instability (so regardless of the level of disturbance) and lead directly to a nonlinear steep-fronted global mode; and, second, that there is a weak stabilizing effect as the steep front to the nonlinear global mode approaches the edge of the disk, which might explain some reports of higher transition Reynolds numbers when located close to the edge.

Table 3 shows the transition Reynolds number in recent studies measured using a hot-wire probe listing the stated transition Reynolds numbers in ascending order. The previous authors used different definitions for the transition Reynolds number, however, and the present data will be compared with each definition.

Lingwood (1995, 1997) suggested that the local absolute instability appears above $R = 507$ and that it triggers nonlinearity and the onset of transition. In the present paper, the transition Reynolds number, R_t, is defined as the onset of nonlinearity where the peak amplitude of the first harmonic of the primary vortices reaches 10^{-6} in terms of the ensemble-averaged power spectrum intensity of the azimuthal velocity. The power spectrum is defined as $P(\omega^*) = (2/N_{FFT}^2)\,|H(\omega^*)|^2$, where $H(\omega^*)$ is the discrete Fourier transform of the time series and the normalization factor is $N_{FFT} = 2048$, which is the number of data points in one period of each discrete Fourier transform in this study. While the transition Reynolds number definition used here relies on the peak value of the first harmonic reaching the threshold of 10^{-6}, there is no qualitative change in behaviour if the mean amplitude within a frequency range centred on the first harmonic peak is used instead.

https://doi.org/10.1017/jfm.2012.564 Published online by Cambridge University Press

https://doi.org/10.1017/jfm.2012.564 Published online by Cambridge University Press

Authors	R_t	The definition of R_t	R_{tn}
Lingwood (1996)	508 : (502–514)	Onset of nonlinearity	508 : (502–514)
Malik *et al.* (1981)	520 : (513–526)	First formation of locally turbulent regions	<460 rough-disk convective route
Othman & Corke (2006)	539	Onset of deformation of laminar profile	515 : (505–526)
Wilkinson & Malik (1985)	550 : (543–556)	Turbulent breakdown preceded by secondary instability	515 : (488–543)
Kobayashi *et al.* (1980)	566	Entire loss of periodic velocity fluctuations	<500 rough-disk convective route

TABLE 3. Experimental transition Reynolds numbers, R_t (as defined in the original studies by previous authors using hot-wire anemometry), listed in ascending order of stated transition Reynolds number. In some cases, as in Healey (2010, table 1), the mid-point between two measurement Reynolds numbers is given. Note that Healey (2010, table 1) gives 500 as the transition Reynolds number of Kobayashi *et al.* (1980) as an estimation of their onset of nonlinearity; R_t is given here as 566 as stated in Kobayashi *et al.* (1980) original paper and their definition is summarized, as well as providing a reinterpreted transition Reynolds number, R_{tn}, in the fourth column, based on onset of nonlinearity.

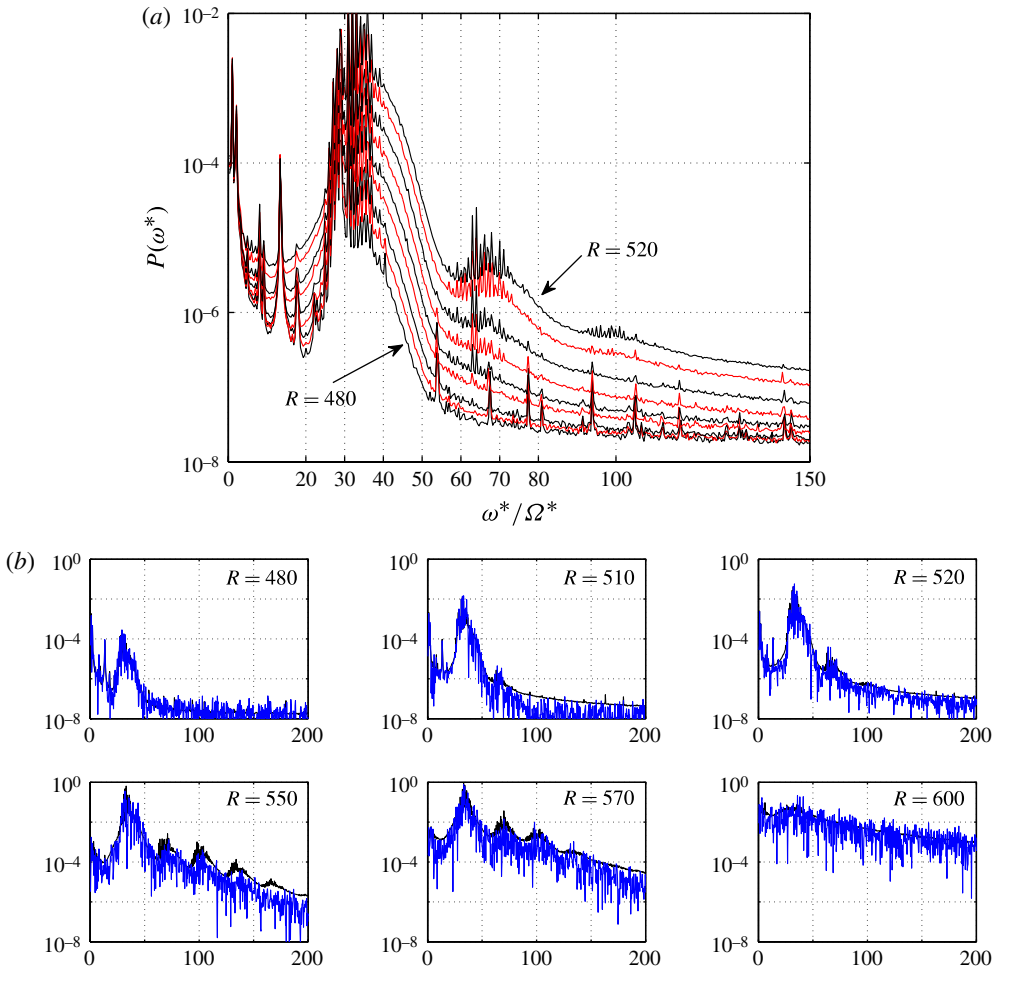


FIGURE 6. (Colour online) Spectra measured at $z = 1.3$ (IP04). (*a*) Ensemble-averaged spectra $P(\omega^*)$ at 5 ΔR intervals between $R = 480$ and $R = 520$. (*b*) Single-realization power spectra for arbitrarily selected series of 2048 data points (with corresponding-ensemble averaged spectra shown as a solid line) at $R = 480, 510, 550, 570$ and 600 measured at $z = 1.3$ (IP04).

Figure 6 shows an example of the transition Reynolds number definition of the ensemble-averaged power spectrum. At $R = 480$ the spectrum due to the primary vortices appears at around $\omega^*/\Omega^* = 31$ and the spectrum band for the primary vortices expands with increasing Reynolds number. This result corresponds to figure 6 in Malik *et al.* (1981) so that the number of vortices increases as a function of Reynolds number. The peak around $\omega^*/\Omega^* = 1$ is due to imbalance of the disk. At $R = 500$, nonlinearity starts to cause harmonics of the primary vortices to appear at around $\omega^*/\Omega^* = 63$. At $R = 510$, the amplitude of the harmonics reaches 10^{-6} in the power-spectrum scale. With this definition (in agreement with Lingwood 1996), the onset of the transition is suggested as $R_t = 510$, which corresponds to assuming, as in Healey (2010) and Pier (2003), that the onset of transition occurs at the steep-fronted nonlinear global mode located at the convective–absolute

https://doi.org/10.1017/jfm.2012.564 Published online by Cambridge University Press

transition boundary, and (as in Healey 2010) setting a somewhat arbitrary amplitude threshold corresponding to near the base of the front. As shown by Lingwood (1996), nonlinear interactions modify the stationary disturbances (which are repeatably excited by unavoidable roughness on the surface of the disk) and, therefore, both single-realization and ensemble-average data lead to the same identification of the first onset of nonlinearity (initiation of the nonlinear global mode) and to the definition of the transition Reynolds number used here. The subplot for $R = 510$ in figure 6(*b*) shows the emergence of the harmonic clearly in both the single-realization and ensemble-averaged spectrum. Other researchers listed in table 3 have, as discussed below, used alternative definitions for the transition Reynolds number, which result in higher stated values of the Reynolds number and demark later stages of the laminar–turbulent transition process.

At $R = 550$ through to $R = 600$ in figure 6(*b*), which spans the strongly asymmetric region in the p.d.f. maps of figure 5, the spectra fill out fully; comparing well with Viaud *et al.*'s (2011) figures 4 and 5, where they observed a primary nonlinear global front, followed by a region of exponential growth, and then by a secondary front where the spectrum fills out (which they suggest indicates absolute instability of the saturated primary instability to secondary instabilities leading directly to spatial and temporal disorder). Here, the secondary front appears at a Reynolds number of about 550, characterized by a change in slope of the v_{rms} profiles in figure 4 and the appearance of skewness in figure 5, giving a higher threshold that, it is suggested, marks the onset of secondary instability. The fully turbulent boundary layer is not realized until the Reynolds number reaches about 650 (Imayama *et al.* 2012).

The transition Reynolds number for Wilkinson & Malik (1985) is given as 550, corresponding to a position at 0.945 of the disk radius. This is the mid-point (between 543 and 556) of the range within which they saw turbulent breakdown (and by their definition located R_t) and led Healey (2010) to locate a point in his figure 7(*b*) suggesting that their transitional Reynolds number was stabilized by the proximity to the edge of the disk. However, their transition Reynolds number is defined towards the upper bound on the transitional region, coming after secondary instability has been observed (see their conclusions, for example), hence in table 3 Wilkinson & Malik's (1985) stated transition Reynolds number is described as the point where turbulent breakdown (preceded by secondary instability) is observed. It is not possible to determine precisely from Wilkinson & Malik's (1985) presented data at what Reynolds number the first signs of nonlinearity are observed, but it is somewhere between 488 and 543 (515 average) where the peaks in their figure 11 become sharper, putting the radius at the transition Reynolds number at between 0.865 and 0.878 of the disk radius. Table 3 gives this reinterpreted transition Reynolds number in the final column.

Malik *et al.*'s (1981) earlier experiments used the same disk apparatus as Wilkinson & Malik (1985), i.e. with the same disk radius and same overhanging flow-control panel, but Wilkinson & Malik (1985) mounted the disk more conventionally on a vertical axis and had a smoother disk surface. Malik *et al.* (1981) report the first formation of locally turbulent regions (and by their definition located R_t) between 513 (0.911 of the disk radius) and 526 (0.934 of the disk radius), averaging 520. In the present experiments, occasional wavepackets were observed for $R < 550$, appearing non-periodically and non-repeatably and seeming to be due to dust falling from above and either being carried through the boundary layer without attaching or becoming attached to the surface. At higher Reynolds numbers these occasional wavepackets had turbulent characteristics but at $R = 520$ there was a very low probability of

https://doi.org/10.1017/jfm.2012.564 Published online by Cambridge University Press

turbulent-spot formation. From this, the turbulent spots observed by Malik *et al.* (1981) at around $R = 520$ are supposed to be a result of large initial disturbances.

Furthermore, from the evidence presented in Malik *et al.* (1981) it is suggested that their figure 3 shows the start of amplitude saturation at about 460 and, therefore, necessarily the onset of nonlinearity at even lower Reynolds numbers. Malik *et al.*'s (1981) figure 3 closely resembles Wilkinson & Malik's (1985) rough-disk experiments; see, for example, their figure 16. Wilkinson & Malik (1985) state (in their conclusions) that the rough-disk experiments gave rise to localized turbulent bursts between 521 and 530 (averaging 526) (rather than the 543–556 (averaging 550) they observed for turbulent bursts for the 'clean' disk); again similar to Malik *et al.*'s (1981) first formation of locally turbulent regions between 513 and 526. Healey (2010) suggests in explanation of his figure 7(*b*) that Malik *et al.* (1981) might be showing a case of transition via convective instability given it was a relatively rough disk compared with (the clean-disk experiments of) Wilkinson & Malik (1985) and that the global mode front of his theory represents an upper bound on the onset of transition, i.e. the highest transition Reynolds number obtainable for a 'clean' disk. This suggestion seems to be borne out by the evidence and here the reinterpreted transition Reynolds number in table 3 is given as less than $R = 460$, via a rough-disk convective route.

Othman & Corke (2006) define the transition Reynolds number as the onset of deformation of the laminar azimuthal velocity profile due to nonlinearity, giving $R_t = 539$ (at 0.918 of the disk radius). Healey (2010) treated the onset of mean-flow distortion as equivalent to onset of nonlinearity (and equivalently 'onset of transition'). While this equivalence is justifiable, Othman & Corke (2006) are likely to have observed the onset of mean-flow distortion below $R = 539$. They based the identification of mean-flow distortion on their plots of mean azimuthal velocity profiles, which seems to show that the distortion first begins somewhere between 526 and 539, although this is known not to be a sensitive indicator of the first signs of nonlinearity. However, Othman & Corke's (2006) figure 5 shows the appearance of the first harmonic in the spectra at $R = 505$ and more clearly at $R = 514$ and 526, which also suggests a lower quantitative value should be given for the onset of nonlinearity/transition for comparison with the present results. Othman & Corke's (2006) figure 7 shows radial growth in amplitude of some selected frequencies and, while somewhat subjective, the saturation appears around 520. Here, the reinterpreted transition Reynolds number for Othman & Corke (2006) in table 3 is given as lying between 505 and 526 (averaging 515).

Kobayashi *et al.*'s (1980) figure 9 shows a time series at $R = 500$, which is described as lying within the region of nonlinear oscillations, that is strongly transitional (much more so than would be expected from clean-disk experiments). It is suggested here that these experiments fall into the rough-disk category and the onset of nonlinearity/transition is at a Reynolds number less than 500 (closer estimation of the first onset of nonlinearity is not possible to determine from the presented data), and is via a convective route as with Malik *et al.* (1981) (with Healey's (2010) edge-induced global mode front representing an upper bound on the onset of transition for clean-disk experiments). Here, the reinterpreted transition Reynolds number for Kobayashi *et al.* (1980) in table 3 is given as less than $R = 500$, via a rough-disk convective route. (Note that both Kobayashi *et al.* (1980) and Malik *et al.* (1981) are the oldest of the hot-wire experiments reported and both mounted their disks 'unconventionally' on a horizontal shaft.)

https://doi.org/10.1017/jfm.2012.564 Published online by Cambridge University Press

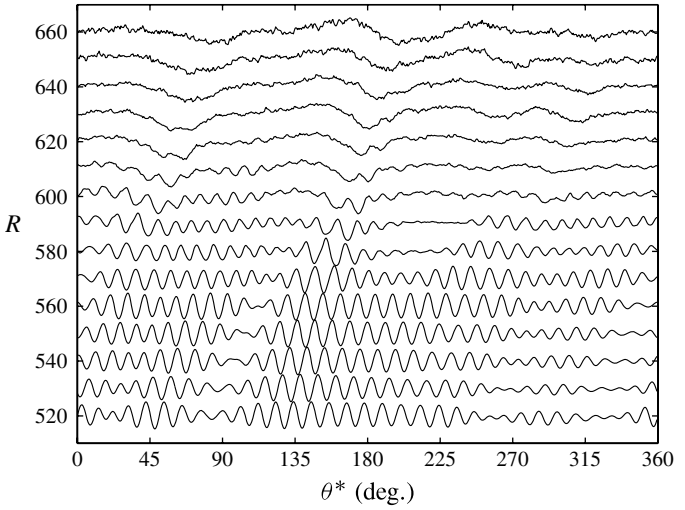


FIGURE 7. Ensemble-averaged time series of the azimuthal velocity at various measurement Reynolds numbers at $z = 1.3$ for plate type (IP04). The signals are normalized by the maximum peak-to-peak amplitude. Measurements are taken in the laboratory frame of reference.

To look briefly at the later stages of the transition process, figure 7 shows ensemble-averaged time series of peak-normalized azimuthal velocity (averaged over 1000 revolutions) at 10 ΔR intervals. At $R = 520$ in figure 7 approximately 33 stationary oscillations are observed per rotation; these are the primary vortices, see figure 2 in Kohama (1984). Between $R = 520$ and 560 the amplitudes of the primary vortices differ. This is because the disturbance field is a superposition created by a random distribution of unavoidable surface roughness. The breakdown of the stationary modes starts to appear in these ensemble-averaged time series at $R = 580$, $\theta^* = 190$–$230°$. Note that single-realization time series would show the beginnings of breakdown at a lower Reynolds number but ensemble-averaged data show more easily the last remnants of periodicity (which will be the remnants of periodic stationary disturbances in the absence of repeatable excitation of unstable travelling disturbances). The stationary modes are shown here to lose all periodicity at $R = 620$–630. The observed Reynolds number for the breakdown and the entire loss of periodicity here is much larger than that of Kobayashi *et al.* (1980) and Wilkinson & Malik (1985).

The effect of the edge Reynolds number on the transition Reynolds number is shown in figure 8. The transition Reynolds numbers with different edge Reynolds number and edge configurations from the present experiments are plotted against the edge Reynolds number, together with the prediction of the edge effect of Healey (2010) and the data from other authors that he presented in his figure 7(*b*). The results from the present study show a lack of dependence of R_t on these edge configurations and edge Reynolds number, and the reinterpreted transition Reynolds numbers (using a consistent definition) from previous studies also align with the present results or, in the case of Kobayashi *et al.* (1980) and Malik *et al.* (1981), suggest an alternative convectively unstable rough-disk route to turbulence.

https://doi.org/10.1017/jfm.2012.564 Published online by Cambridge University Press

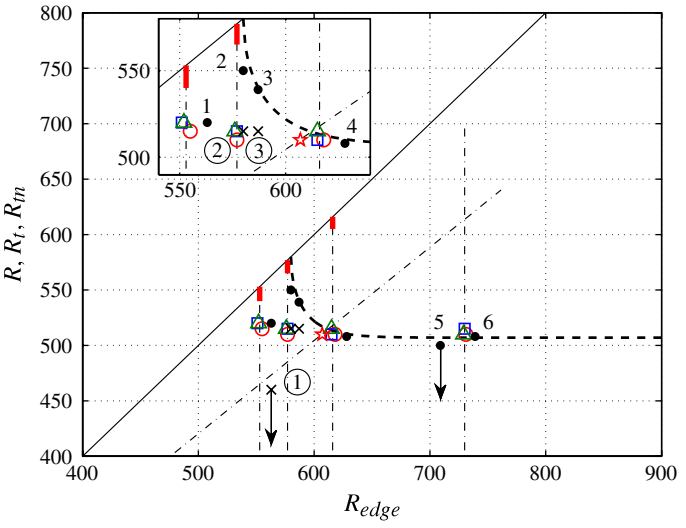


FIGURE 8. Dependence of R_t (as defined here) on the Reynolds number at the edge of the disk, R_{edge} with different edge conditions: □, open type, IO01-04; △, ring type, IR01-04; ○, plate type, IP01-04; and ☆, IP00. Chain lines mark R_{edge} for the Reynolds numbers at which measurements were taken for the various cases shown (as given in table 2). Three vertical thick lines close to the diagonal represent the region of approximately $12\Delta R$ very close to the edge of the disk where velocity measurements (beyond those points shown in figure 2) are excluded. The solid line and dashed line represent, respectively, the boundary of the edge, i.e. where $R_t = R_{edge}$ and the edge effect suggested by a flow model using the complex Ginzburg–Landau equation taken from Healey (2010). The numbered dots, 1–6, indicate the transition Reynolds numbers given by Healey's (2010) figure 7(*b*) using other authors' experimental data as presented there in table 1: 1 is Malik *et al.* (1981), 2 is Wilkinson & Malik (1985), 3 is Othman & Corke (2006), 4 and 6 are Lingwood (1996), 5 is Kobayashi *et al.* (1980), respectively. These data points correspond to the R_t column of table 3 here apart from the transition Reynolds number for Kobayashi *et al.* (1980) which is shown in this figure at $R_t = 500$ to compare with Healey's (2010) figure 7(*b*). The circled numbers, ①–③, indicate the reinterpreted transition Reynolds numbers presented in the R_{tn} column of table 3: ① is Malik *et al.* (1981) showing (with the arrow) the onset of nonlinearity and transition at a Reynolds number somewhere below 460, and 5 is Kobayashi *et al.* (1980) showing (with the arrow) the onset of nonlinearity and transition somewhere below 500; as discussed in § 4.

5. Conclusions

An experimental study has been performed to investigate the laminar–turbulent transition process of a rotating-disk flow with different edge conditions and different edge Reynolds numbers. Three different edge configurations were studied and four different edge Reynolds numbers with each edge configuration. The results with different edge conditions are shown to agree closely. The open type has the largest background-noise level compared with the ring and plate types. This is because the eight aluminum components fixing the glass to the aluminum-alloy disk generate a disturbances field with eight oscillations per rotation of the disk. However, the varying background-noise levels in this study are not observed to affect to the transition process in a significant way. This result is reinforced by the p.d.f. maps shown in figure 5, which graphically reveal the transition process described further in Imayama *et al.* (2012). The p.d.f. maps showing a superposition of measurements with the four

https://doi.org/10.1017/jfm.2012.564 Published online by Cambridge University Press

different edge Reynolds numbers are continuous (with one small exception), which indicates that R_{edge} does not affect the transition process significantly.

The transition Reynolds number, R_t, is defined here as the onset of nonlinearity where the peak amplitude of the first harmonic of the primary vortices reach 10^{-6} in terms of the ensemble-averaged power spectrum intensity of azimuthal velocity, as shown in figure 6. Measurements were taken all of the way to the disk edge (IO01-03, IR01-03, IP01-03), but data where the mean velocity was affected were not used (up to approximately 12 ΔR from the disk edge, see table 2. This is as close as Othman & Corke (2006) and closer than Wilkinson & Malik (1985) and yet the transition Reynolds number as a function of the edge Reynolds number, which is represented in figure 8, showed no discernible dependence, i.e. were found to be in the range $510 \leqslant R_t \leqslant 520$.

Healey's (2010) figure 7(*b*) predicts R_t increasing as R_{edge} approaches R_t. This is a qualitative fit to other authors' data and he recognizes that in order to make a quantitative prediction for the dashed curve in his figure 7(*b*), it would be necessary to consider the basic flow near, and beyond, the edge of the disk or that it may be more appropriate to match the global mode to a solution existing in the flow off the edge of the disk. Careful experiments have been undertaken to determine the influence of the disk edge and found that his suggested correlation between R_t and R_{edge}, if present, is weak. Further experiments would be required to quantify any weak correlation.

Excluding the two cases with rough disks that would appear to represent a convectively unstable route to turbulence, the transition Reynolds number obtained (using a consistent definition and listed in figure 8 is $508 \leqslant R_{tn} \leqslant 515$. The already small scatter in observed transition Reynolds numbers for clean disks is reduced by application of a consistent definition. This highly reproducible transition Reynolds number supports the hypothesis of Lingwood (1995) that local absolute instability leads to the onset of nonlinearity and transition. Furthermore, it is also in accordance with the hypothesis of Healey (2010) that the finite disk (present in all experiments) that allows the local absolute instability from linear stability theory to lead to (supercritical) linear global instability and then to a nonlinear steep-fronted global mode.

Further experiments are planned to investigate the suggested convectively unstable route to turbulence for rough disks below the threshold for edge-induced global instability, which Healey (2010) shows represents an upper bound on the onset of transition, i.e. the highest transition Reynolds number obtainable for a 'clean' disk.

Acknowledgements

We are grateful to the Swedish Research Council (VR) and KTH for support of this research. We thank the late Dr T. Nickels who arranged the loan for the experimental apparatus from the University of Cambridge Department of Engineering to KTH. We also would like to thank Dr N. Tillmark, G. Rådberg and J. Karlström for help with preparing the experiment. We would also like to thank the referees for their careful and thoughtful consideration of this paper.

REFERENCES

CHIN, D.-T. & LITT, M. 1972 An electrochemical study of flow instability on a rotating disk. *J. Fluid Mech.* **54**, 613–625.

CLARKSON, M. H., CHIN, S. C. & SHACTER, P. 1980 Flow visualization of inflexional instabilities on a rotating disk. *AIAA Paper* 80-0279.

https://doi.org/10.1017/jfm.2012.564 Published online by Cambridge University Press

COBB, E. C. & SAUNDERS, O. A. 1956 Heat transfer from a rotating disk. *Proc. R. Soc. Lond. Math.* A **236**, 343–351.

DAVIES, C. & CARPENTER, P. W. 2003 Global behaviour corresponding to the absolute instability of the rotating-disc boundary layer. *J. Fluid Mech.* **486**, 287–329.

FEDOROV, B. I., PLAVNIK, G. Z., PROKHOROV, I. V. & ZHUKHOVITSKII, L. G. 1976 Transitional flow conditions on a rotating disk. *J. Engng Phys. Thermophys.* **31**, 1448–1453.

GREGORY, N., STUART, J. T. & WALKER, W. S. 1955 On the stability of three-dimensional boundary layers with application to the flow due to a rotating disk. *Phil. Trans. R. Soc. Lond.* **248**, 155–199.

GREGORY, N & WALKER, W. S. 1960 Experiments on the effect of suction on the flow due to a rotating disk. *J. Fluid Mech.* **9**, 225–234.

HEALEY, J. J. 2010 Model for unstable global modes in the rotating-disk boundary layer. *J. Fluid Mech.* **663**, 148–159.

HUERRE, P. & MONKEWITZ, P. A. 1990 Local and global instabilities in spatially developing flows. *Annu. Rev. Fluid Mech.* **22**, 473–537.

IMAYAMA, S., ALFREDSSON, P. H. & LINGWOOD, R. J. 2012 A new way to describe the transition characteristics of a rotating-disk boundary-layer flow. *Phys. Fluids* **24**, 031701.

JOHANSSON, A. V. & ALFREDSSON, P. H. 1982 On the structure of turbulent channel flow. *J. Fluid Mech.* **122**, 295–314.

VON KÁRMÁN, T. 1921 Über laminare und turbulent Reibung. *Z. Angew. Math. Mech.* **1**, 233–252.

KOBAYASHI, R., KOHAMA, Y. & TAKAMADATE, C. 1980 Spiral vortices in boundary layer transition regime on a rotating disk. *Acta Mech.* **35**, 71–82.

KOHAMA, Y. 1984 Study on boundary layer transition of a rotating disk. *Acta Mech.* **50**, 193–199.

LE GAL, P. 1992 Complex demodulation applied to the transition to turbulence of the flow over a rotating disk. *Phys. Fluids* A **4**, 2523.

LINGWOOD, R. J. 1995 Absolute instability of the boundary layer on a rotating disk. *J. Fluid Mech.* **299**, 17–33.

LINGWOOD, R. J. 1996 An experimental study of absolute instability of the rotating-disk boundary-layer flow. *J. Fluid Mech.* **314**, 373–405.

LINGWOOD, R. J. 1997 Absolute instability of the Ekman layer and related rotating flows. *J. Fluid Mech.* **331**, 405–428.

LINGWOOD, R. J. & GARRETT, S. J. 2011 The effects of surface mass flux on the instability of the BEK system of rotating boundary-layer flows. *Eur. J. Mech. (*B/*Fluids*) **30**, 299–310.

MALIK, M. R., WILKINSON, S. P. & ORSZAG, S. A. 1981 Instability and transition in rotating disk flow. *AIAA J.* **19**, 1131–1138.

OTHMAN, H. & CORKE, T. C. 2006 Experimental investigation of absolute instability of a rotating-disk boundary layer. *J. Fluid Mech.* **565**, 63–94.

PIER, B. 2003 Finite-amplitude crossflow vortices, secondary instability and transition in the rotating-disk boundary layer. *J. Fluid Mech.* **487**, 315–343.

SMITH, N. H. 1947 Exploratory investigation of laminar-boundary-layer oscillations on a rotating disk. NACA TN 1227.

THEODORSEN, T. & REGIER, A. A. 1944 Experiments on drag of revolving disks, cylinders and streamline rods at high speeds. NACA Rep. 793.

VIAUD, B., SERRE, E. & CHOMAZ, J.-M. 2011 Transition to turbulence through steep global-modes cascade in an open rotating cavity. *J. Fluid Mech.* **688**, 493–506.

WILKINSON, S. P. & MALIK, M. R. 1985 Stability experiments in the flow over a rotating disk. *AIAA J.* **23**, 588–595.

https://doi.org/10.1017/jfm.2012.564 Published online by Cambridge University Press